Angular distribution of photons from the decay of the GDR in hot and rotating light Yb nuclei from exclusive experiments

A. Maj [1], J.J. Gaardhøje, A. Ataç [2], S. Mitarai [3], J. Nyberg [4], A. Virtanen [5]

Niels Bohr Institute, Blegdamsvej 15–17, 2200 Copenhagen, Denmark

A. Bracco, F. Camera, B. Million, M. Pignanelli

Dipartimento di Fisica, Universita di Milano e INFN Sezione di Milano, 20133 Milan, Italy

Abstract

Angular distributions of photons associated with the damping of excited-state giant dipole resonances (GDR) in hot and rotating ^{161,162}Yb nuclei have been measured in exclusive experiments using the HECTOR array. In reactions with heavy ions (^{48}Ti) angular distributions are determined as a function of the angular momentum of the compound nuclei. In reactions with lighter ions (^{17,18}O) a difference method is applied to isolate GDR decays originating from specific excitation regions. The systematics of the measured angular distributions as a function of excitation energy and angular momentum are compared to theories taking into account fluctuations of the shape and orientation of the excited nuclei.

1. Introduction

Giant dipole resonance (GDR) high-energy photon spectroscopy has in the course of the past decade established itself as one of the principal tools to study

---

[1] Permanent address: Niewodniczański Institute of Nuclear Physics, 31-342 Kraków, Poland.
[2] Present address: Department of Radiation Sciences, Uppsala University, S-175121 Uppsala, Sweden.
[3] Permanent address: Kyushu University, Fukuoka, Japan.
[4] Permanent address: The Svedberg Laboratory, Uppsala University, S-75121 Uppsala, Sweden.
[5] Permanent address: University of Jyväskylä, Department of Physics, Jyväskylä, Finland.
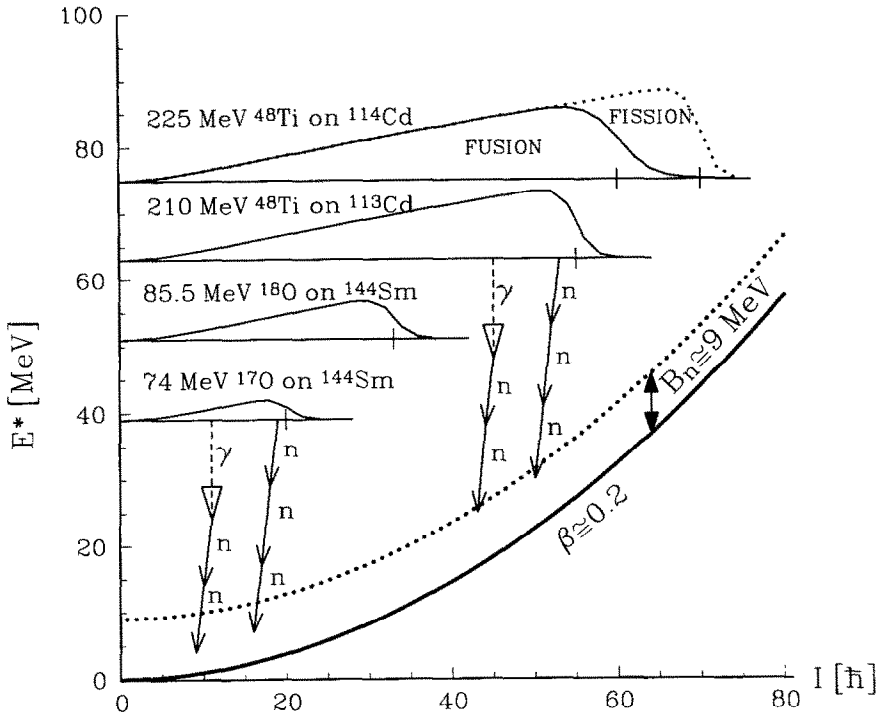
Fig. 1. Schematic diagram showing the decay of the compound nuclei discussed in this article. The used reactions, and in each case the initial excitation energy and calculated initial angular momentum distribution are indicated. The shown yrast line is calculated assuming the rigid-body moment of inertia for a nucleus with $A = 160$ and deformation $\beta = 0.2$.

the properties of highly excited and rotating atomic nuclei [1,2] providing the means to explore the entire phase space available to their decay (see Fig. 1). The sensitivity arises from the fact that the properties of the giant dipole resonance are strongly modified by the quadrupole deformation of the nucleus, wherefore a mapping of the properties of the GDR as function of the excitation energy and angular momentum of the emitting nucleus yields information on the changes of the nuclear properties as these conditions are varied.

Of significant interest is the study of the region of excitation energies ranging from close to the yrast line, where quantal features dominate, to the liquid-drop region where nuclei to a large extent can be described with the use of classical and macroscopic concepts. The transition between these two regimes is thought on quite general grounds to be associated with a transition of the shapes of nuclei, from the shell structure driven ground-state shapes (for example prolate with significant deformation) of strongly interacting many-body systems consisting of identical particles to the oblate shapes of deformable classical objects.

The task of tracing the gradual decline and fall of nuclear shell structure in hot nuclei, has however proven to be more complicated than first expected. The reason is that fluctuations play an important role in describing the properties of hot nuclei, due to the finite number of the constituent particles. Fluctuations lead to a smoothing of many features (for example of the sharp phase transition of the equilibrium deformation of nuclei which is predicted to occur as a function of temperature) and require the interpretation of observables through comparison to model calculations properly averaged over the explored regions of phase space.

The role of shape fluctuations in hot nuclei is strikingly demonstrated by the measured spectra of the GDR in excited and deformed nuclei, which turn out to be much more structureless than for the corresponding cold nuclei [3–9]. The important role of orientation fluctuations is apparent in the measured angular distributions of the photons in the GDR region, which normally have small magnitudes (with the exception of the highest angular momenta as we will discuss in more detail in this article). The interplay between fluctuations of the shape and fluctuations of the orientation relative to the direction of the angular momentum vector will in general not be trivial. While for a rigid body the total angular momentum vector is always parallel to the rotational frequency vector, this is not the case for a deformable body or for a body with a complicated internal structure (gyroscope in classical physics). A further element involved in the understanding of the measured GDR angular distributions is the extent of the coupling of the GDR to the fluctuating atomic nucleus, as expressed through the relative *time scales* associated on the one hand with the fluctuations and on the other hand with adjusting the GDR properties to the fluctuating quantities.

It is no simple experimental task to disentangle these various effects. The heavy-ion reactions that must be used to synthesise hot nuclei in the laboratory produce such nuclei with a wide distribution of angular momenta. Furthermore the GDR gamma rays of interest are emitted at all steps in the nuclear decay sequence, although with decreasing probability the more the nucleus cools. Inclusive measurements lead to a further averaging over large areas of the (I, E^*) space, reducing the experimental sensitivity to the changing nuclear properties.

In this article we present exclusive measurements, using the HECTOR array, of the angular distribution of the GDR photons originating from the decay of hot and rotating ^{161,162}Yb nuclei produced under various conditions using light and heavy ions (sects. 2 and 3). We discuss the results in the context of current theories of shape and orientation fluctuations (sect. 4). The exclusive measurements are of two kinds: (i) as a function of the angular momentum in reactions leading to the formation of compound nuclei with angular momenta up to the fission limit and at various excitation energies and (ii) employing a difference method to isolate decays originating from selected regions of excitation energy. This paper represents part of a larger systematic program that we have undertaken to study the properties of hot nuclei in the $A = 110$ and $A = 160–175$ regions using exclusive experimental techniques.

2. Experimental method

2.1. The HECTOR array

The experiments discussed in this article were carried out with the HECTOR (High Energy deteCTOR) array which is shown in Fig. 2. This detector system is the result of a collaborative project between the University of Milano and the Niels Bohr Institute and is presently operating at the Tandem & Heavy Ion Booster accelerator of the Niels Bohr Institute.

HECTOR consists primarily of eight large single scintillator crystals * of Bariumdifluoride (BaF_2) of 145 mm in diameter and 175 mm in length encased in a lightweight fiberglass housing. The crystals can contain a large fraction of the electromagnetic shower from photons with energies up to 100 MeV. Each crystal is coupled to a single fast photomultiplier tube (EMI 9823Q of diameter 125 mm with a quartz window and selected on stability, rise time and energy resolution) attached to an active voltage divider circuit [10]. The detectors are operated at distance of 30 cm from the target to the front face of the scintillator crystal. This distance represents a compromise between the following requirements: largest possible solid angle for gamma-ray detection, ability to suppress particle induced events by a measurement of the time of flight from the target, and negligible summing (i.e. probability for 2 gamma rays or 1 gamma ray and 1 neutron from the same event to interact in the same detector within the pulse integration time). The detectors are normally equipped with 6 mm Pb absorbers in order to eliminate most of the low-energy gamma rays ($E_\gamma < 1$ MeV) from the target thereby further reducing summing effects. In the experiments discussed here the detectors were positioned mostly at angles $\alpha = \pm 160°$, $\pm 130°$, $\pm 90°$ and $\pm 50°$ with respect to the beam direction, permitting to measure angular distributions. In a part of the experiments one detector was placed at 0°. The detectors are found to have identical response functions over the entire energy range of interest. The response is reflected in measured angular distribution patterns $A_2(E_\gamma)$ (see sect. 3) almost only as 1 MeV rigid shift of the pattern down the energy axis.

HECTOR is also equipped with a multiplicity array (see Fig. 2). In the case of the experiments reported here it consisted of 14 BaF_2 (50 mm diameter and 50 mm in length) located at approximately 5 cm from the target. This array has since been upgraded [11] to a close-packed "castle" consisting of 38 hexagonal sticks of BaF_2. The array serves as a time trigger for the time-of-flight measurements and allows to measure the average angular momentum of the residues from the reaction (see next section). The excellent time resolution of the set-up (Δt (FWHM) ≈ 0.6 ns) is displayed in Fig. 3. It allows an essentially perfect separation of neutrons and

---

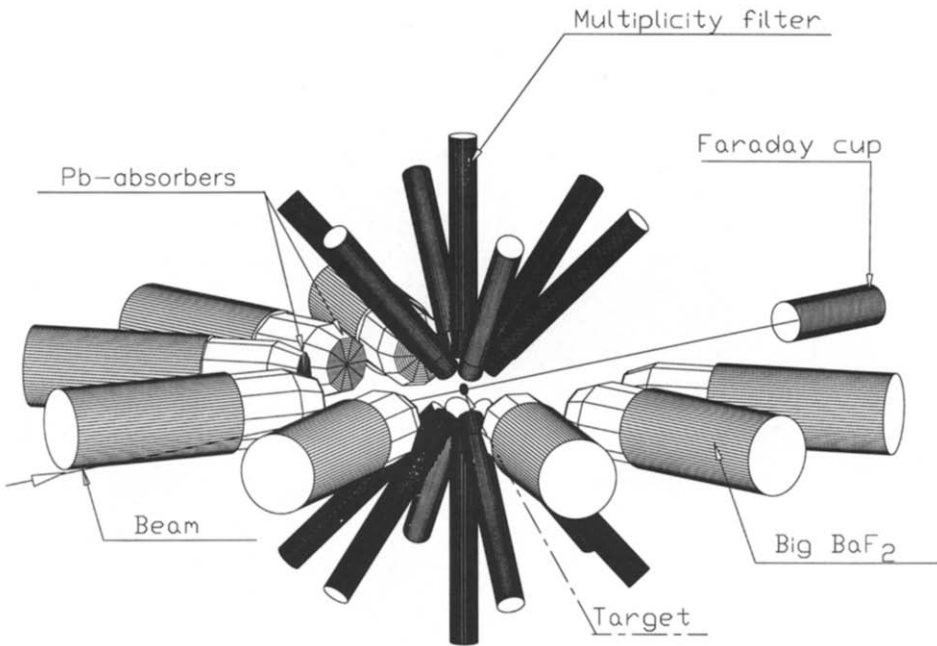* Produced and delivered by Karl Korth, Kiel, Germany.

Fig. 2. The experimental configuration of the HECTOR array used in the experiments described in sect. 2. Photons in the energy range 5–40 MeV emitted at different angles are measured in the large BaF$_2$ scintillators located at 30 cm from the target. The multiplicity array, consisting of 14 smaller BaF$_2$ scintillators, is used to determine the angular momentum of the fusion residues and also serves as a fast time trigger.

gamma rays. The contribution to the total spectrum from gamma rays, neutrons and background is shown in Fig. 4.

The dependence of the relative intensities of the two scintillation components of BaF$_2$ (220 and 320 nm) on the type of interaction (electronic or heavy charged particle) permits a discrimination against charged particles (p, d, α...) by an analysis of the pulse shape. In the present case the fast component was integrated using a 30 ns wide gate while the entire pulse was integrated using a gate with a width of 1 μs. At the bombarding energies relevant here the contribution to charged particles was minimal. The pulse shape analysis is nevertheless still useful as an additional veto against pile up events as schematically illustrated in Fig. 5.

The energy calibration of the BaF$_2$-detectors was done by measuring the 6.13 MeV γ-rays from a Pu^{13}C radioactive source in the low-energy range and the 15.1 MeV γ-rays produced in the ^{2}H(^{11}B, nγ)^{12}C reaction in the GDR region. The used charge sensitive ADC's sense and correct for any charge presented to the device outside of the pulse duration thus ensuring zero offsets of the calibration. The energy resolution, for the typical bias voltage used (around 1400 V), was 7–8% at 6.1 MeV.
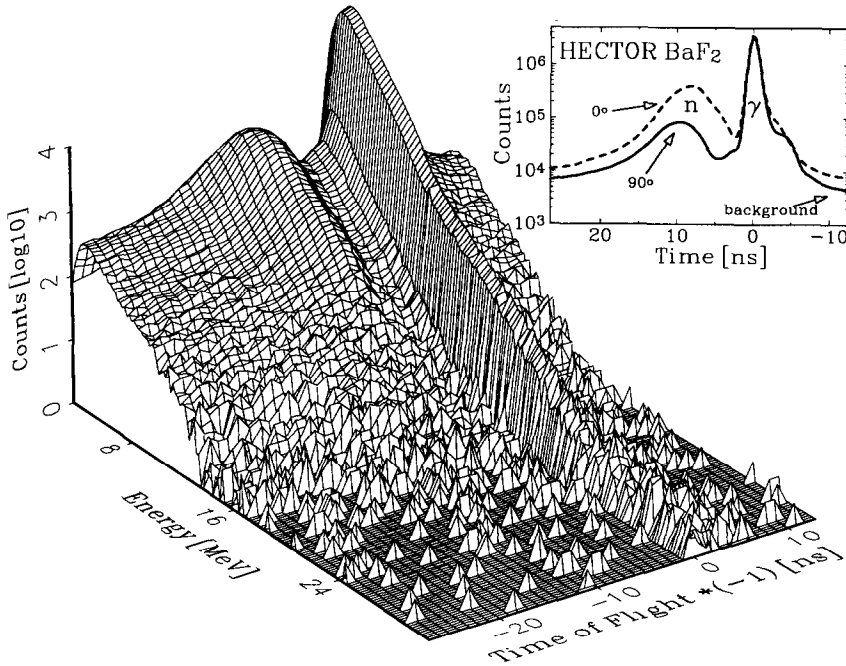
Fig. 3. Two-dimensional time-of-flight versus energy spectrum in a large BaF$_2$ detector (in this case located 90° with respect to the beam direction at 30 cm from the target) measured relative to the time trigger provided by the BaF$_2$ multiplicity array (operated in OR condition). In the inset a projection of this spectrum on the time axis is compared to the projection when the detector was moved to 0°. Gamma-ray (γ) and neutron (n) events are clearly separated. The shoulder on the right side of the γ-peak is due to imperfect electronics. The detection threshold for high-energy gamma rays was ≈ 4 MeV.

The gain stability of the detectors was monitored by feeding to the detectors a well-defined light pulse from a common temperature stabilised light emitting diode (LED) through optical fibres. The rate of the signal was kept at approximately 10 Hz. The shape of the LED peak in the spectrum is shown in the left-hand side of Fig. 6. Any gain drifts were corrected in the off-line analysis on a 5–6 minute basis by comparing the centroid of the LED peak sampled over approximately 3000 events to a reference position. Gain variations were corrected with an accuracy better than 0.15%. A typical behaviour of the detector gain is illustrated in the right-hand side of Fig. 6, where the position of the LED-peak is shown as a function of time. It is found that most of the short time gain variations can be correlated with variations in the beam intensity. Long term drift is mainly associated with changes in ambient temperature. Due to the stable temperature of the target room long term drift is generally small.

Fig. 7 shows the logic's of the fast and slow electronics and of the data acquisition system. Events were defined by requiring a coincidence between a
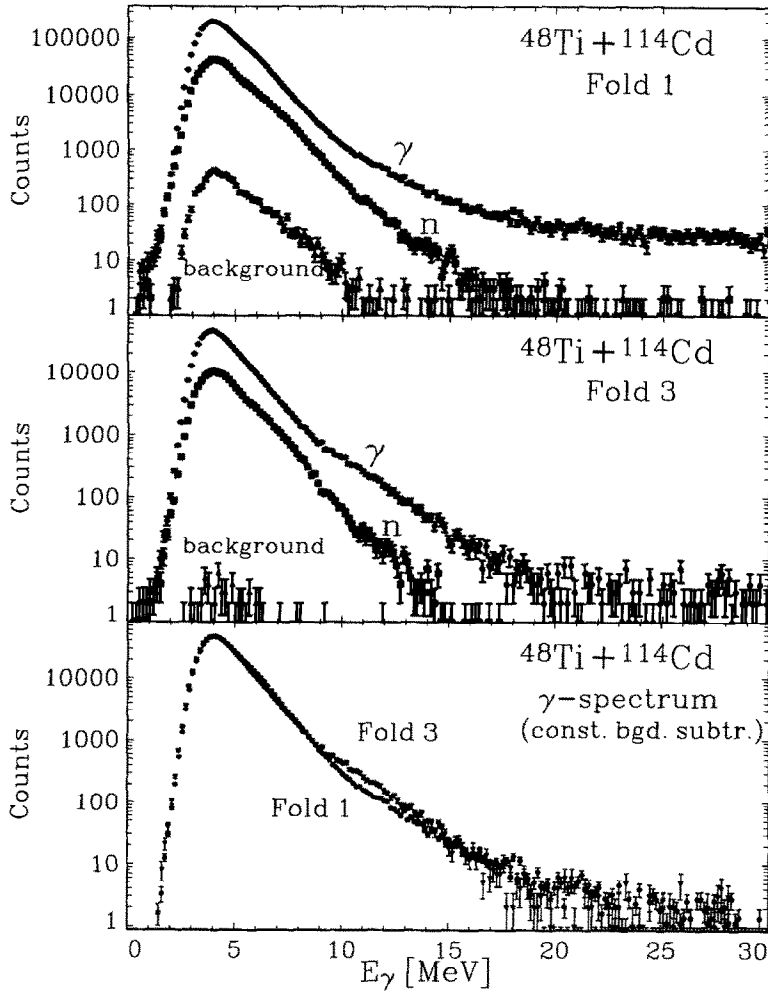
Fig. 4. Shape and relative intensity of the contribution from gamma rays, neutrons and background events to the total gamma-ray spectrum as determined by setting gates of equal width on the appropriate parts of the time spectrum shown in Fig. 3. The two top panels correspond to a further requirement of detecting 1 and 3 low-energy gamma rays in the multiplicity array respectively. The lower panel shows a comparison between the gamma-ray spectra corresponding to folds 1 and 3 after subtracting a constant residual background at high energies (mostly due to cosmic rays).

pulse with $E_\gamma > 4$ MeV in any of the large BaF_2 detectors and a pulse with $E_\gamma > 150$ keV in any of the detectors of the multiplicity array. The resulting logic signal is further OR'ed with a logic signal from the LED and with a signal from the OR of the multiplicity filter (with a downscaled rate). This trigger signal is used to gate the QDC's and TDC's (in CAMAC) and the computer system. The data acquisition system is based on a number of Motorola 68010 processors operating in
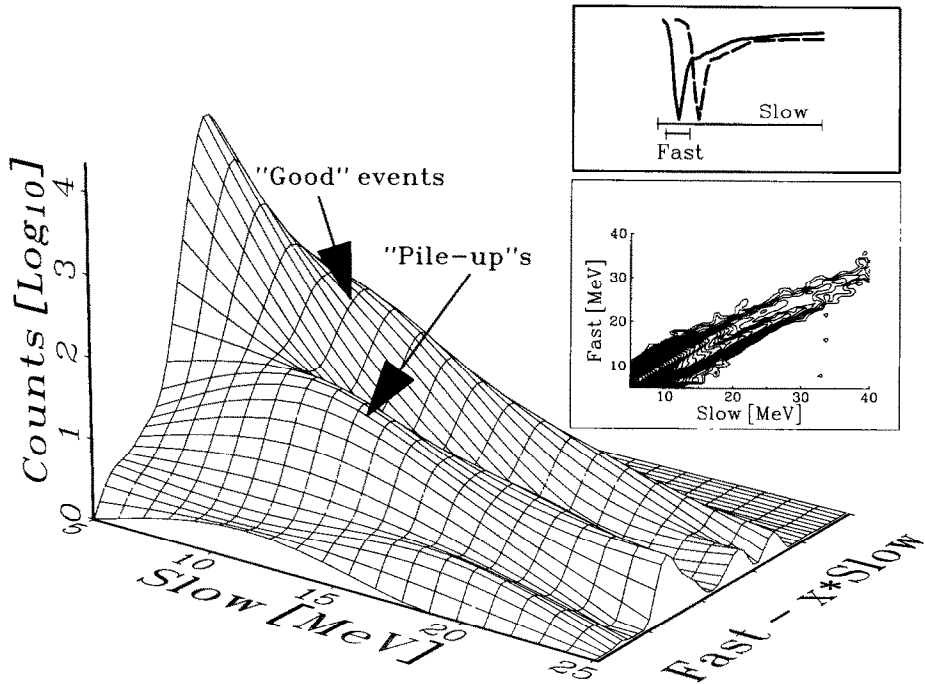
Fig. 5. Illustration of pulse-shape discrimination obtained by applying two gates of different width to the energy pulse of a BaF$_2$ detector (in this case located at 0°) and integrating the charge in each window (see top inset). Since the detectors are operated in air the contribution from charged particles is normally modest and the main purpose of the pulse-shape discrimination is to reduce pile-up. The lower inset shows a projection of the three-dimensional distribution.

parallel in a VME environment [12]. Formatted events are transmitted to the main VAX 8650 where on-line histogramming (1D and 2D), display, experiment control and storage on Exabyte magnetic tapes occurs. In the present experiments coincidence event rates of 1000 events/s were common, although the acquisition system can handle rates up to about 5000 events/s without significant deadtime.

The downscaled rate of the BaF$_2$ multiplicity array (LE γ-rays) is used to estimate the absolute number of high-energy gamma rays per energy bin that are emitted for each fusion reaction (multiplicity of HE γ-rays). Indeed, the ratio of the rate of *coincidence* events and of the rate of *singles* events (LE events), corrected for the finite solid angle of the HE detectors (dω/dΩ) and for the scale down factor F of the singles rate, is equal to the ratio of the cross section for HE gamma-ray emission divided by the fusion cross section, and thus also equal to the multiplicity of HE gamma rays in the considered interval of gamma-ray energies centered around E_γ

$$\frac{R(\text{HE}\gamma \wedge \text{LE}\gamma)}{R(\text{LE}\gamma) \cdot F} \left(\frac{d\omega}{d\Omega}\right)^{-1} = \frac{\sigma_\gamma(E_\gamma)}{\sigma_{\text{Fus}}} = \frac{dM_{\text{HE}\gamma}(E_\gamma)}{dE_\gamma}$$
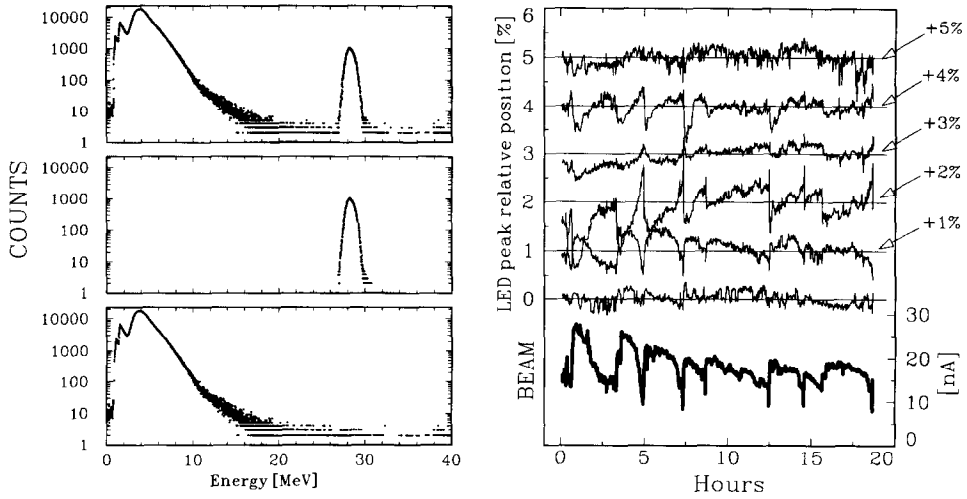
Fig. 6. Illustration of the gain monitoring and stabilisation procedure. The left side of the figure shows the peak appearing in the spectrum from a HECTOR BaF$_2$ detector arising from the light pulse from a common temperature stabilised LED. The contributions from reaction events and LED events can be separated by requiring coincidence and anti-coincidence with the LED signal respectively (middle and lower left panels). The right side of the figure shows the time dependence of the centroid position of the LED peak as a function of time for various detectors, and for comparison the corresponding fluctuations in beam intensity.

We note that this procedure has the advantage of being independent of dead time and of variations in beam intensity, target thickness etc. It is a number that can be directly compared to the results of statistical model calculations. We remark that the assumption that the singles rate of the multiplicity array is proportional to the rate of fusion reactions may only be valid above a certain fold.

2.2. Determination of angular momentum distributions

With the used geometry the efficiency of the 14 element multiplicity array was experimentally determined be to be close to 19% and the scattering probability between neighbouring detectors to about 5%. The response, i.e. the conversion of measured fold to multiplicity was established using a method similar to that described by Jääskeläinen et al. [13]. In brief, the method consists of recording gamma rays from a radioactive source emitting two gamma rays in cascade (e.g. ^{60}Co, ^{207}Bi) and located at the target position. One of the large volume BaF$_2$ detectors is used as a trigger, and the events are considered only if the 1.33 MeV gamma-ray from the ^{60}Co source (1.06 MeV or 1.77 MeV in the case of ^{207}Bi) results in a full energy peak, ensuring that exactly one gamma-ray (1.17 MeV for ^{60}Co or 570 keV for ^{207}Bi) is presented to the multiplicity filter. With this condition events consisting of the analogue signal from the Multiplicity Unit (see

Fig. 7) proportional to the number of firing detectors (i.e. fold), are stored on tape. The 0-fold events, corresponding to situations where the gamma-ray exposed to the filter escape without interaction, are also included. Hence the measured fold spectrum is the response of the filter to gamma-ray multiplicity $M = 1$ (at the specific energy 1.17 MeV or 570 keV). The response to multiplicity $M = k$ is generated, in the off-line analysis, by randomly selecting k events from the tape and summing up the amplitudes of the associated individual fold-signals. The response matrix obtained in this way for gamma rays with an average energy of 1.17 MeV is shown in Fig. 8, assuming a production cross section for the various multiplicities with a triangular shape, as is the case for fusion reactions.

The fold to multiplicity conversion can also be calculated using a simple recursive algorithm proposed by Holm [14] for the probability $P(F, M)$ of triggering F out of N detectors by a cascade of M γ-rays using as input the experimentally determined total efficiency Ω and scattering probability ϵ:

$$P(F, M) = a_F P(F, M-1) + b_F P(F-1, M-1) + c_F P(F-2, M-1)$$

with

$$a_F = 1 - (N-F)\omega\left(1 + \epsilon\frac{F}{N-1}\right),$$

$$b_F = (N-F+1)\omega\left(1 - \epsilon\frac{N-2F+1}{N-1}\right),$$

$$c_F = (N-F+2)\omega\epsilon\frac{N-F+1}{N-1},$$

$P(F, M) = 0$ for $F < 0$ or $M < 0$, $P(0, 0) = 1$ and $P(F, 0) = 0$. The detection efficiency of each detector is ω, i.e. $N\omega = \Omega$.

Fig. 9 shows the angular momentum distributions for different folds (assuming the relation $I = 2M$). These distributions are practically identical to those that can be obtained from the "experimental" response matrix shown in Fig. 8.

Apart from allowing a study of the angular momentum dependence of the GDR, the selection on different fold regions is important for discriminating against low multiplicity events associated with non-fusion or background events. The importance of the latter is exhibited in Fig. 4. It is apparent that the high-energy gamma-ray spectra gated by fold 1 contain a large background. The spectra associated with the higher folds are much cleaner. In the lower panel of Fig. 4 we compare spectra gated by folds 1 and 3 after subtraction of residual linear backgrounds. We find apart from the natural angular momentum dependence a somewhat anomalous behaviour of the spectrum corresponding to fold 1 events (shoulder in spectrum at $E_\gamma \approx 6$–7 MeV and significant high energy
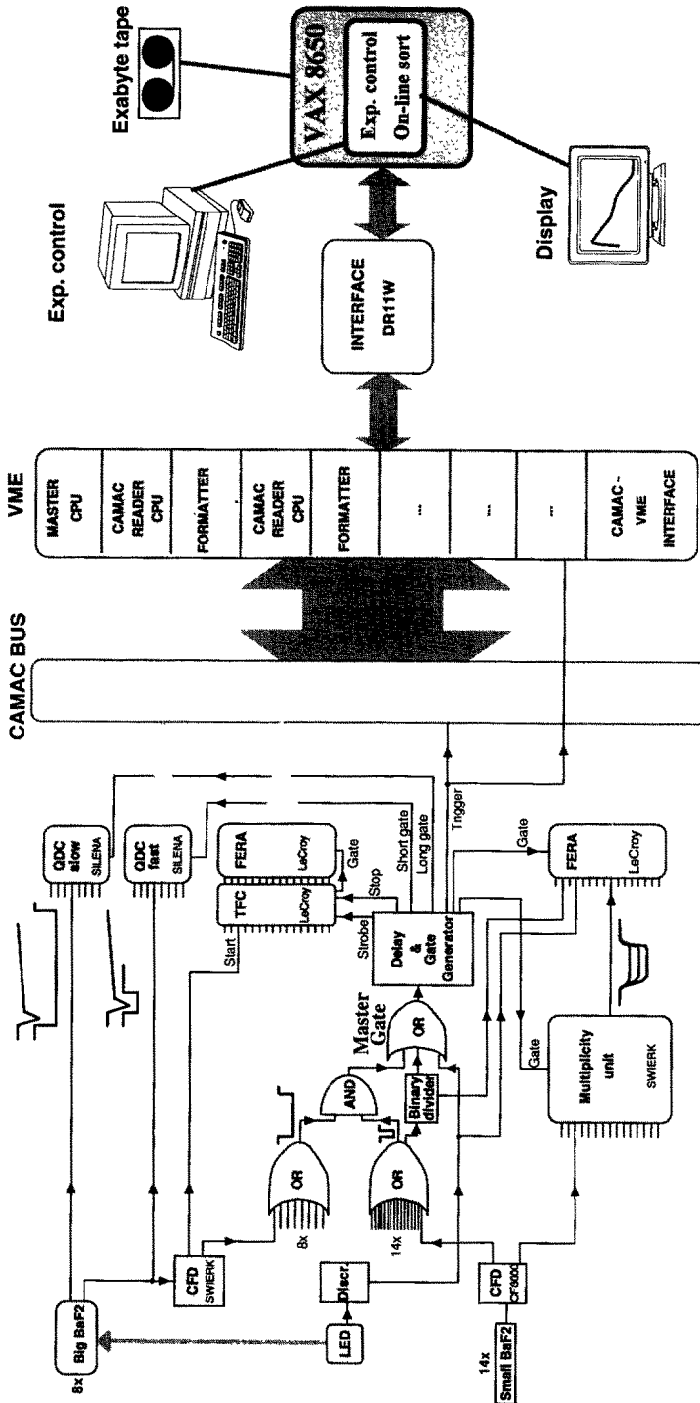
Fig. 7. Schematic layout of the electronics and data acquisition logic. The event definition requires the detection of an interaction depositing $E > 5$ MeV in one of the big BaF_2 and the participation of at least one small BaF_2 detector.
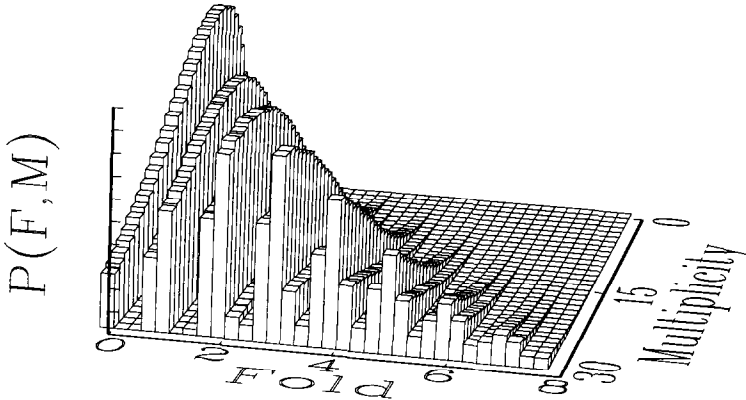
Fig. 8. Illustration of the fold to multiplicity response (i.e. the probability $P(F, M)$ in arbitrary units of triggering F detectors by M gamma rays) of the used multiplicity array. The response matrix has been determined by constructing synthetic high multiplicity events using the measured response (analogue signal from the Multiplicity Unit) to ^{60}Co gamma rays. The multiplicity distribution has been assumed to have a triangular shape.

background, see also Fig. 11). We associate these features with non-fusion events. We consequently consider fold 1 events only with some reserve in the following.

3. Angular distribution of GDR photons from exclusive experiments

Fig. 10 illustrates schematically how the angular distribution of the GDR photons depends on the nuclear properties, in particular the deformation and shape. The insets in the figure show the expected behaviour of the magnitude of the $B[E1](E_\gamma)$ matrix elements and of the $A_2(E_\gamma)$ coefficients (see definition in sect. 3.1) as a function of the gamma-ray energy in the transition-energy region of the GDR for 4 different shapes of the same deformation (here chosen to be $\beta = 0.3$). The different nuclear shapes are characterised by the elongation parameter β and the triaxiality parameter γ. The grid shows calculated contours of the free energy as a function of these quantities. In the figure we have used the convention that $\gamma = 0°$ denotes a prolate nucleus rotating collectively (i.e. around an axis perpendicular to the symmetry axis), $\gamma = -60°$ an oblate nucleus rotating non-collectively (i.e. around an axis parallel to the symmetry axis), $\gamma = 60°$ an oblate nucleus rotating collectively and finally $\gamma = 120°$ a prolate nucleus rotating non-collectively.

The GDR strength functions calculated for these well-defined nuclear shapes have characteristic fine structures arising from the superposition of the contributions from vibrations along each of the principal axes of the nucleus (with frequencies inversely proportional to the length of the axes). In addition, the
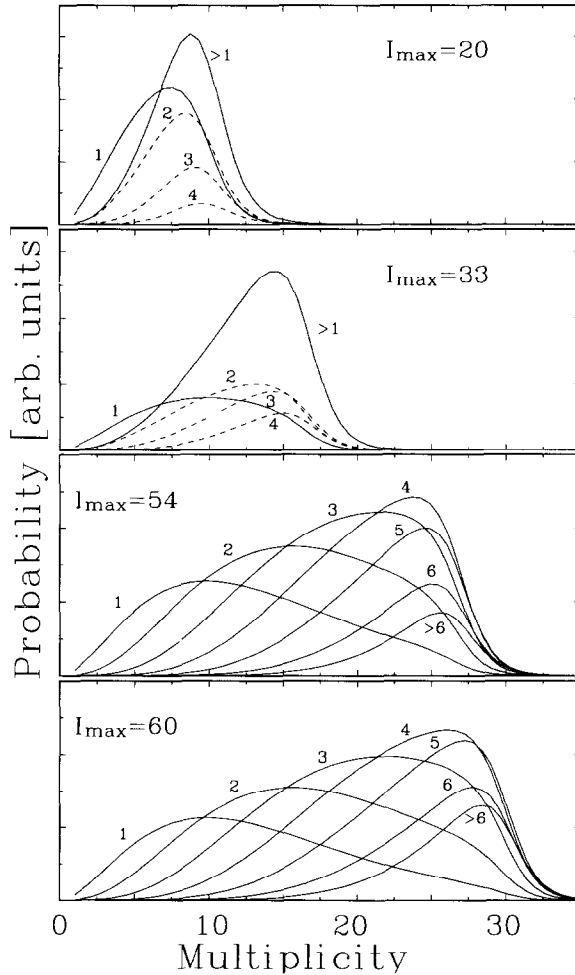
Fig. 9. Calculated multiplicity distributions for various folds for the oxygen and titanium induced reactions based on the experimentally determined efficiency of the multiplicity array. The curves have been folded with the cross section dependence of the input multiplicity distribution.

angular distribution of gamma rays shows a characteristic pattern that contains information on the orientation of the nucleus with respect to a given axis, for example an axis parallel to the direction of the total angular momentum vector. This is due to the fact that the GDR components corresponding to vibrations along the principal axes of the nucleus have different angular distributions in the laboratory frame of reference, depending on whether the considered vibration is parallel or perpendicular to the direction of the total angular momentum vector.

The magnitude of *measured* GDR angular distributions reflects not only one shape, but rather, in the case of significant shape fluctuations, the extent and form
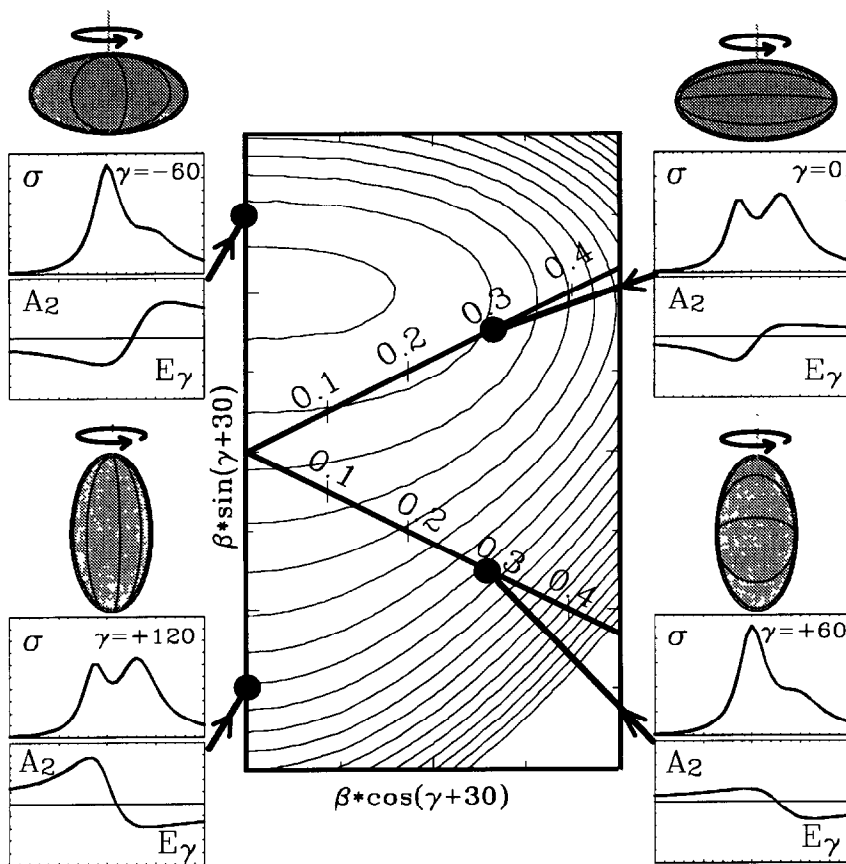
Fig. 10. Schematic illustration of the GDR strength function and angular distribution as a function of gamma ray energy for nuclei of a fixed deformation ($\beta = 0.3$) but of various shapes. Shape and orientation fluctuations sampling all or part of the available phase space in the quadrupole deformation and orientation variables lead to much smoother effective strength functions and normally to reduced angular distributions.

of the shape ensemble at the given E^* and I and to what extent the GDR couples to the different deformations. In the case of an *adiabatic coupling* of the GDR to the quadrupole degrees of freedom, the effective GDR angular distribution will reflect the ensemble of different shapes. Also, fluctuations in the angle between the symmetry axis of the nucleus and the direction of the total angular momentum affect the angular distribution by reducing its amplitude. We will discuss these issues in more detail in sect. 4.

3.1. Angular distributions in $^{161,162}Yb$ as a function of angular momentum

Fig. 11 shows measured GDR gamma-ray spectra from the reaction ^{48}Ti + ^{114}Cd at E(beam) = 225 MeV leading to ^{162}Yb nuclei at $E^* = 70$ MeV. The spectra are

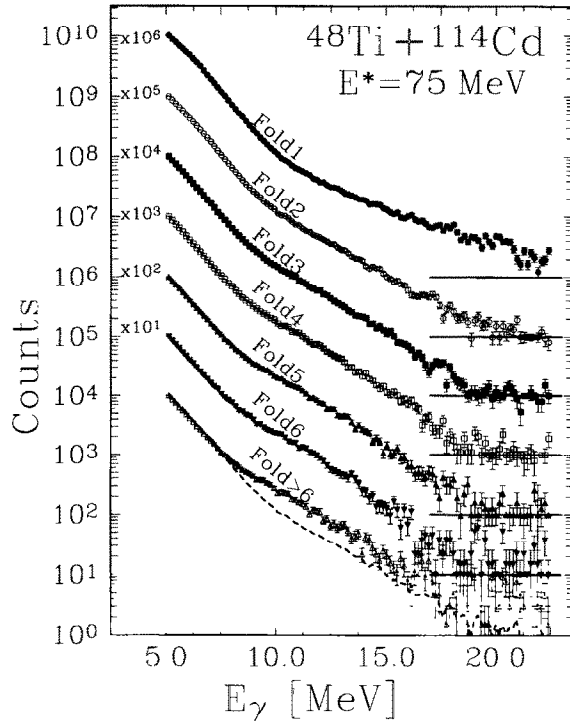Fig. 11. Measured gamma-ray spectra from the reaction ^{48}Ti$+^{114}$Cd $\rightarrow$ ^{162}Yb gated by different folds. The spectra, normalised to fold > 6 at $E_\gamma = 6$ MeV, are shifted along the ordinate by a factor of 10 relative to each other. The average angular momentum corresponding to each spectrum is listed in Table 2. The spectrum corresponding to fold 2 is compared to the spectrum for fold > 6 (dashed line).

obtained by gating on different folds (1–7) measured in the multiplicity array. Spectra corresponding to detectors located at different angles have been added. To be noted is the overall similarity of spectra corresponding to fold > 1. A closer inspection reveals, however, significant and systematic variations in the GDR region as a function of fold (see for example the comparison of spectra corresponding to folds 2 and > 6 in fig. 11 and of folds 1 and 3 in Fig. 4). As previously mentioned spectra corresponding to fold 1 deviate significantly at $E_\gamma > 15$ MeV from the spectra corresponding to folds > 1. Table 1 lists information relevant to the reactions discussed in this article. Table 2 lists the average angular momentum associated with each fold gate obtained by the methods discussed in sect. 2. Also listed in Table 2 are the standard deviations and skewness coefficients of the multiplicity distributions (see also Fig. 9).

Fig. 12 shows the distribution of the $A_2(E_\gamma)$ coefficients for ^{161}Yb and ^{162}Yb for the different spin regions, in the reactions using ^{48}Ti beams. These distributions were obtained in the following way. For each of the 8 detectors two-dimensional spectra of gamma-ray energy as a function of fold were sorted, with appropriate

Table 1
Summary of properties of the compound nuclei produced in the light- and heavy-ion-induced reactions discussed in this article. The table lists the beam energy, target thickness and isotopic purity, the maximum excitation energy, the calculated maximum transferred angular momentum and the fusion cross sections (see also Fig. 1). For the last reaction is indicated also the angular momentum l_{fiss} for which fission begins to dominate over the particle emission

Reaction	E(beam) [MeV]	Target [mg/cm^2]	E^*(max) [MeV]	l_{max} [$\hbar$]	σ(fusion) [mb]
^{17}O + ^{144}Sm	74.0	2.2 (96.5%)	38.8	20	270
^{18}O + ^{144}Sm	85.5	2.2 (96.5%)	50.8	33	640
^{48}Ti + ^{113}Cd	210.0	1.3 (93.4%)	62.8	54	400
^{48}Ti + ^{114}Cd	225.0	1.1 (98.7%)	74.8	70 (l_{fiss} = 60)	610

gates on the gamma-ray peak of the TOF spectrum and on the main diagonal of the pulse shape spectrum. Energy spectra corresponding to specific fold intervals were projected (see Table 2). If necessary a constant background, determined as the average number of counts per channel in the energy region 25–30 MeV was subtracted. This background, mostly present in the spectra corresponding to low

Table 2
Correspondence between the measured fold of the low-energy gamma rays detected in the multiplicity array and the average multiplicity (M) of emitted gamma rays, for the studied reactions. Also listed are the estimated average angular momentum of the gamma-ray emitting nucleus, the standard deviation (σ) and the skewness parameter (γ_1) of the associated distribution (see also Fig. 9)

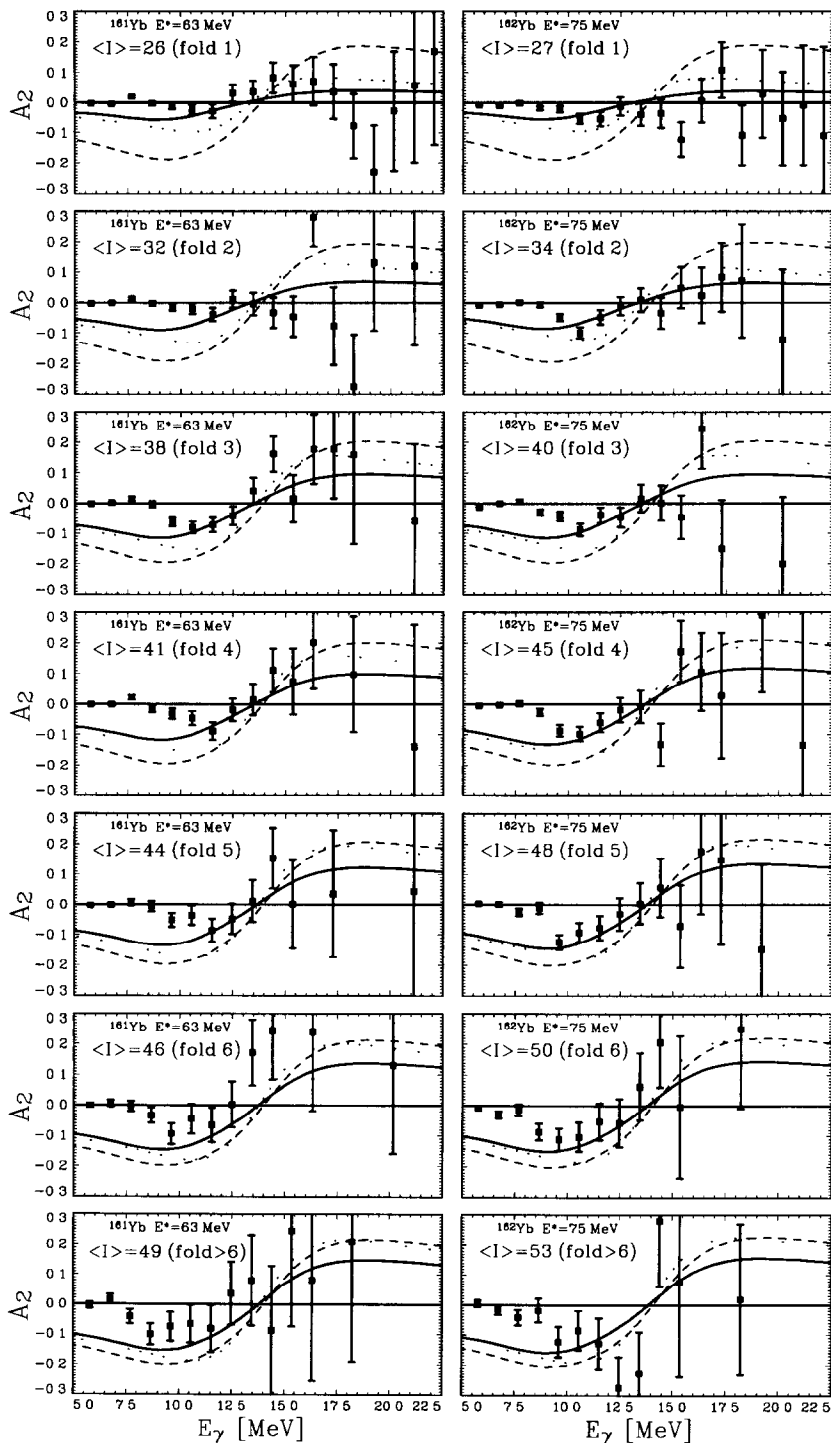| Reaction	Fold	$\langle M \rangle$	$\langle I \rangle$ [$\hbar$]	σ [$\hbar$]	γ_1
^{17}O + ^{144}Sm	> 1	8.4	16.8	4.8	0.00
^{18}O + ^{144}Sm	> 1	12.7	25.4	7.0	−0.14
^{48}Ti + ^{113}Cd	1	12.9	25.8	12.2	+0.24
	2	16.2	32.4	11.8	0.00
	3	18.8	37.6	10.8	−0.16
	4	20.6	41.2	9.6	−0.27
	5	22.0	44.0	8.6	−0.42
	6	23.1	46.2	7.6	−0.66
	> 6	24.3	48.6	6.8	−0.98
^{48}Ti + ^{114}Cd	1	13.4	26.8	13.2	+0.33
	2	17.2	34.4	13.0	+0.04
	3	20.2	40.4	12.0	−0.14
	4	22.3	44.6	10.8	−0.23
	5	24.0	48.0	9.2	−0.38
	6	25.2	50.4	8.6	−0.55
	> 6	26.5	53.0	7.2	−0.72

Fig. 12. Angular distribution coefficients as a function of the gamma-ray energy in the GDR region determined for the reactions ^{48}Ti + ^{113,114}Cd → ^{161,162}Yb for various fold gates. The curves are calculated with a fluctuation theory (see sect. 4) and shifted along the abscissa by -1 MeV in order to take on account the detector's response. See also Figs. 19 and 20.

folds, is thought to originate mainly from random coincidences with cosmic rays. The eight spectra corresponding to different detection angles α with respect to the beam direction were subsequently normalised to each other in the region of statistical gamma-rays: between 5 and 6 MeV. This procedure is based on the
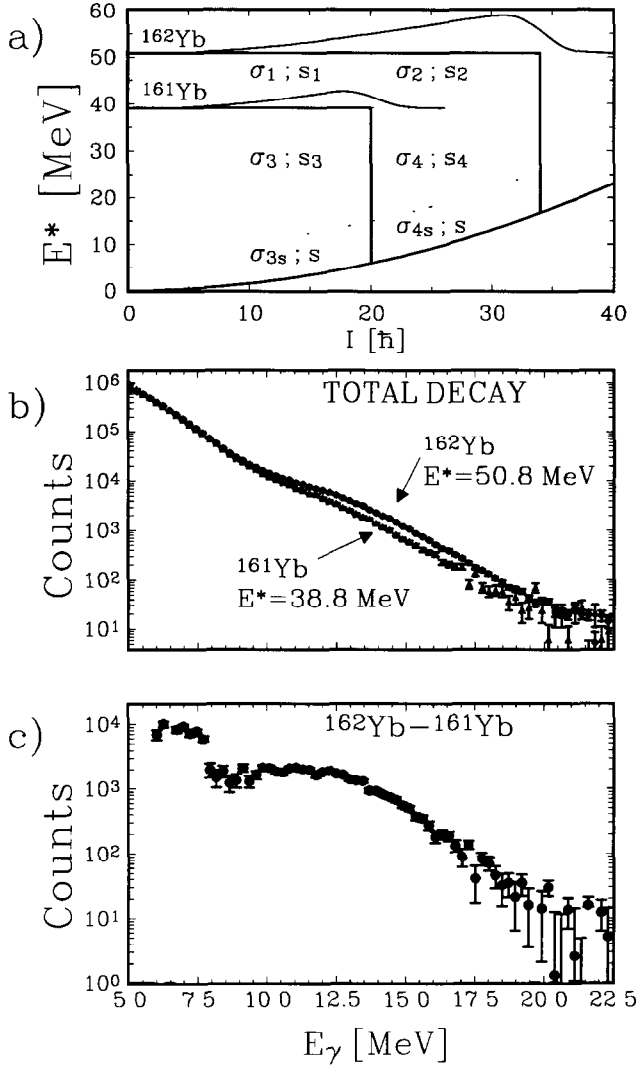

Fig. 13. (a) Schematic illustration of the E^* and I regions populated by the Oxygen induced reactions discussed in this work. Each region is characterised by the cross section for gamma ray emission σ, and the spectrum shape S. The subtraction method isolates the GDR decay from regions 1, 2 and 4. The contribution from region 4 depends on the degree of angular momentum matching obtained in the experiment. (b) Angle-integrated measured gamma-ray spectra from the decay of ^{162}Yb and ^{161}Yb. (c) The difference of the two spectra contains most of the GDR gamma rays at $E_\gamma = 15$ MeV emitted directly from the ^{162}Yb compound nucleus.

results of earlier measurements finding that the gamma rays in this region are emitted almost isotropically [5,7]. One has to point out however that for more quantitative discussion one needs better measurements of the angular distribution of statistical tails. After such a normalisation the spectra were binned to approximately 1 MeV per channel, and the A_2 coefficients for each channel (gamma-ray energy) were determined by a least-squares fit of the number of counts at the different angles to the expression $N(\alpha) = A_0(1 + A_2 \cdot P_2(\cos \alpha))$, where α is the angle between the emitted gamma ray and the beam axis.

The salient features that may be recognised in Fig. 12 are: (i) overall the amplitudes of the A_2 coefficients are small ($< | -0.1 |$, significantly less than the expected $A_2 = -0.25$ for a stretched dipole transition), (ii) the magnitude of the A_2 coefficients increases slowly with increasing angular momentum and (iii) the difference between the angular distributions at each fold (spin) measured for ^{161}Yb (at $E^* = 63$ MeV) and for ^{162}Yb (at $E^* = 75$ MeV) is very small.

Also shown in Fig. 12 are calculations of $A_2(E_\gamma)$ distributions for the relevant (E^*, I) conditions within the framework of fluctuation theories. We will discuss the comparison of experiments and model calculations in sect. 4. The calculated $A_2(E_\gamma)$ patterns were shifted by -1 MeV along abscissa to account the detectors response.

3.2. Angular distribution in ^{161,162}Yb using an energy differential method

In sect. 3.1 we have presented GDR spectra measured as a function of the angular momentum of the compound nucleus. It should be recognised, however, that although this type of experiment represents an improved sensitivity over inclusive measurements sampling the entire (E^*, I) space available for the decay, the measured spectra still contain the sum of all gamma rays competing with particle evaporation and originating from emissions at all steps in the nuclear deexcitation sequence. The consequence is that the measured photon spectra contain information not only on the compound nucleus itself but also on the various daughter nuclei populated at different temperatures. Hence, comparison to model calculations requires an averaging over an ensemble of nuclei which may have quite different properties as a function of temperature. This obviously limits the sensitivity of such comparisons.

In this section we discuss a method to isolate the high-energy gamma rays from the decay of the GDR from specific regions in the (E^*, I) plane, by using an energy difference technique [15,16].

Fig. 13b shows the angle-integrated gamma-ray spectra measured in the two reactions and illustrates the idea of the differential technique. Spectra corresponding to fold > 1 from the decay of ^{162}Yb and ^{161}Yb produced with ^{16,17}O at different E^* (see reaction details in Table 1) are compared. The excitation energy of ^{161}Yb was chosen to be equal to that remaining after the evaporation of the first neutron
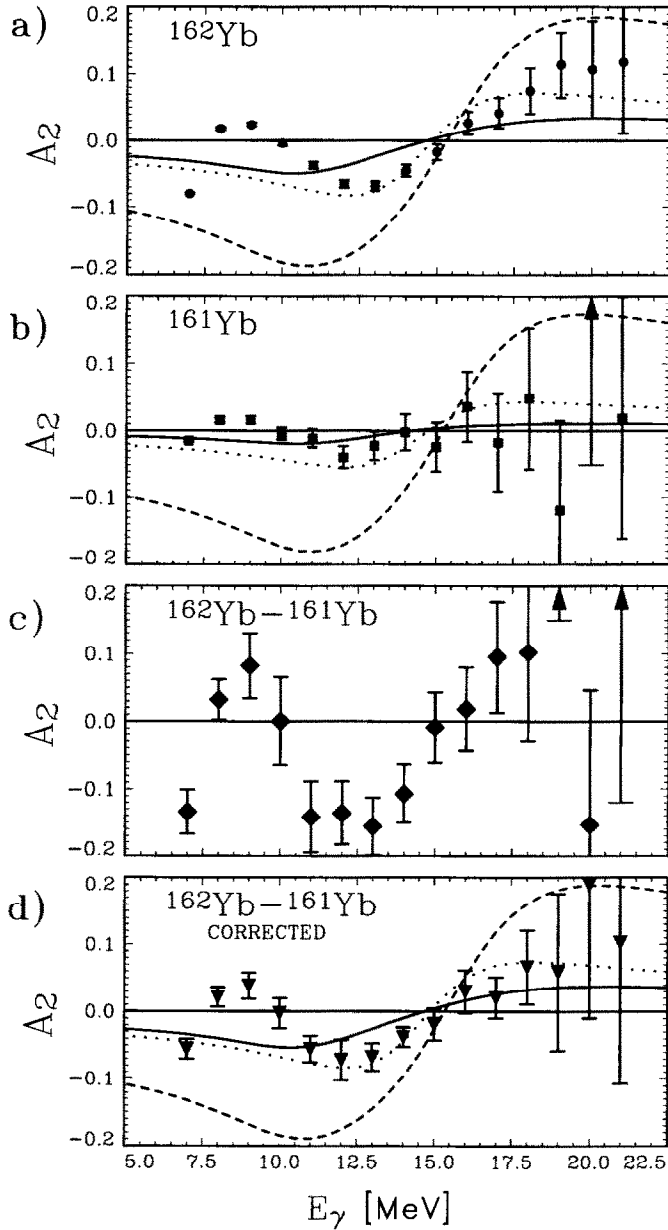
Fig. 14. (a) Measured A_2 distribution for the inclusive decay of ^{162}Yb. (b) Same for ^{161}Yb. (c) A_2 distribution for the difference spectrum obtained as described in the text. (d) Corrected A_2 distribution taking into account the different I regions populated in the reactions. Calculations: adiabatic average over all possible shapes and orientations (full drawn line); equilibrium shape (dotted line); adiabatic average only over possible shapes (dashed line).

from ^{162}Yb. In these nuclei particle evaporation is practically only by neutron emission. Thus, the gamma-ray emission from ^{161}Yb represents the part of the gamma-ray decay which is common to the two reactions. Subtraction of the two spectra thus results in a spectrum of the gamma rays which compete with the first neutron evaporated from the compound nucleus ^{162}Yb.

With this method, the temperature spread of states, on which the GDR is built, is reduced to the width of the GDR itself and to a broadening due to the energy loss of the beam in the target. It therefore becomes possible to isolate GDR gamma-ray emission originating from a specific region of excitation energy.

For such a procedure to be well defined, the angular momentum corresponding to the spectra which are compared must be kept the same. If this is not the case, the difference spectrum will contain contributions from the region of I not common to the two reactions.

As discussed in sect. 2 we do not determine the absolute cross section for gamma-ray emission in the experiments since the fusion cross section is not directly measured. Therefore we have chosen to normalise the gamma-ray spectra from the two reactions to the multiplicity of gamma rays per MeV in the interval $E_\gamma = 6.0$–6.5 MeV, a quantity we can determine in the experiments as discussed in sect. 2.1. The difference spectrum so constructed is shown in Fig. 13c.

In Fig. 14a and 14b we display the A_2 coefficients as a function of E_γ. In Fig. 14c we show the $A_2(E_\gamma)$ distribution for the difference spectrum. It is apparent that the $A_2(E_\gamma)$ coefficients deduced for the difference spectrum are considerably larger than those obtained for either of the inclusive decays. A sizeable part of this is due to the fact that we cannot experimentally match the angular momentum input in these two low angular momentum reactions, as may be seen from the calculated fold to multiplicity response shown in the two top panels of Fig. 9. It is however worth noting that the increase in the size of the $A_2(E_\gamma)$ is in itself evidence for changing nuclear properties as a function of E^* and I.

In the absence of a complete matching of the angular momentum regions covered by the two reactions the difference spectrum will, in addition to the first generation gamma-ray spectra (labelled S_1 and S_2 in Fig. 13a), also contain gamma rays emitted at lower temperature from the region not common to the two reactions (of spectrum shape labelled S_4 in Fig. 13a). Thus the method leads in general to the determination of the properties of $S_1 + S_2 + S_4$. In the following, we present a general method to evaluate the real A_2 coefficients corresponding to such difference spectra.

With the used normalisation procedure, the subtraction of a spectrum of the type measured for the reaction at lower energy, S_3, implies that a fraction $R = \sigma_{4s}/(\sigma_{3s} + \sigma_{4s})$ of S_3 has been oversubtracted, instead of the (unknown) spectrum S_4. Here σ_{3s} and σ_{4s} refer to the cross sections for the emission of the low-energy statistical gamma rays (of identical spectrum shape, S) in the two different I regions. This ratio is proportional to the ratio of the corresponding

fusion cross sections. If both reactions populate the same I interval, $R = 0$. In the limit of very different I distributions, $R \to 1$. If $R \neq 0$, the procedure will affect the deduced A_2 coefficients for the difference spectrum if the properties of the low-spin spectrum are changing with I, i.e. if $S_3 \neq S_4$. We can express the apparent angular distribution coefficients of the difference spectrum, A'_2, in terms of the real A_2 of the difference and the measured coefficients for the low-energy spectrum, A_2^L,

$$
A'_2 = \frac{N^D(0°) - N^D(90°)}{N^D(90°) + 0.5N^D(0°)}
$$

$$
= \frac{1 + A_2 - R(1 + A_2^L) - \left[1 - 0.5A_2 - R(1 - 0.5A_2^L)\right]}{1 - 0.5A_2 - R(1 - 0.5A_2^L) + 0.5\left[1 + A_2 - R(1 + A_2^L)\right]}
$$

$$
= \frac{A_2 - RA_2^L}{1 - R}
$$

where $N^D(\alpha)$ is the number of counts measured in the difference spectrum at the different angles and where R can be calculated from a fusion cross section code.

For the present reactions we calculate $R = 0.66$. This estimate is based on the cross sections associated with the actual I distributions corresponding to the applied gates on the measured gamma-ray fold. According to equation above, this leads to an increase of A'_2, by a factor of approximately 2, as compared to A_2. We remark that while a mismatch in I between the two reactions reduces the sensitivity of the difference method, the contribution from gamma rays with $E_\gamma = 15$ MeV from the *first step* decay to the difference spectrum (regions 1 and 2) is about 77%. This is because "contaminating" gamma decays from region 4 are reduced due to the lower effective level density. In Fig. 14d we display the corrected A_2 distribution. In Fig. 14 we also compare the measured $A_2(E_\gamma)$ to model calculations. This comparison will be discussed in sect. 4.

The measurement of spectra at different angles also provides us with the possibility of analysing the GDR spectrum in a nearly model-independent way (see also ref. [5]). Since radiation of other multipolarities than E1 is expected to be unimportant between 10 and 20 MeV we can uniquely decompose the observed difference spectrum, corrected for the different populated I regions, into the contributions from stretched and unstretched radiation according to

$$
S(\alpha) = \left[1 + \eta A_2^{\Delta I = 0} P_2(\cos \alpha)\right] S^{\Delta I = 0} + \left[1 + \eta A_2^{\Delta I = \pm 1} P_2(\cos \alpha)\right] S^{\Delta I = \pm 1}.
$$

In this analysis $A_2^{\Delta I = 0} = 0.5$ and $A_2^{\Delta I = \pm 1} = -0.25$. The coefficient η has been introduced to take into account the attenuation due to fluctuations of the orientation of the nucleus with respect to the spin direction. We have used $\eta = 0.25$,
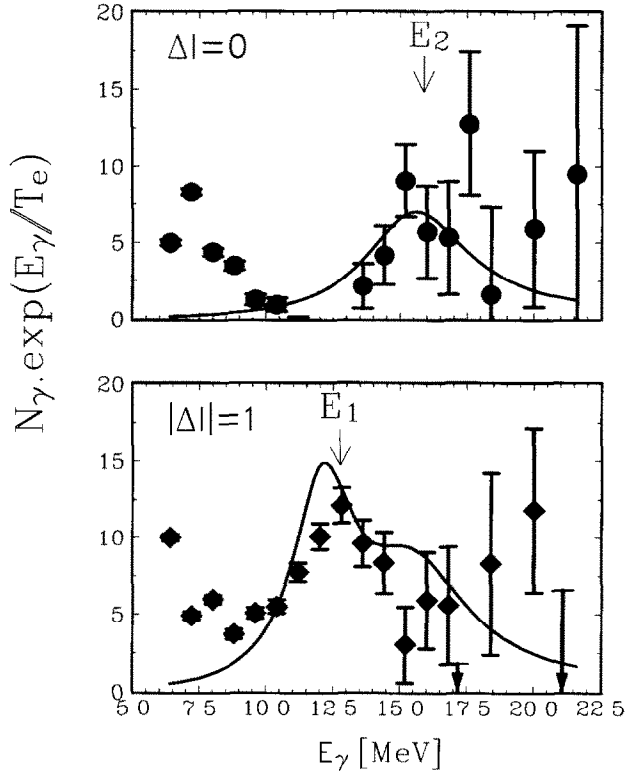
Fig. 15. Decomposition of the gamma rays from the ^{162}Yb compound nucleus in the GDR region in terms of the $\Delta I = 0$ and $\Delta I = \pm 1$ components. Decomposed spectra have been multiplied by exponential function with an effective temperature $T_e = 1.55$ MeV to allow the representation on linear scale. Note that the $\Delta I = 0$ component (top panel) is located in the upper half of the GDR distribution, excluding oblate nuclear shapes rotating collectively. Also shown (lines) is the shape of the $\Delta I = 0$ and $\Delta I = \pm 1$ components obtained in a fit to photo-absorption spectra from cold prolate Er nuclei, using two lorentzians.

deduced from the calculations shown in Fig. 14d and discussed in sect. 4. The main features, however, do not change appreciably as long as η is in the range 0.15–0.45. The result of this procedure applied to the difference spectrum from the oxygen-induced reactions is displayed in Fig. 15. The upper panel shows that the contribution of $\Delta I = 0$ gamma rays to the GDR is localised around $E_\gamma = 16$ MeV. No $\Delta I = 0$ strength is found in the lower part of the GDR distribution as expected for prolate collective or oblate non-collective rotation, and thereby unambiguously excluding oblate collective rotation. The lower part of the figure shows that the $\Delta I = \pm 1$ strength is mostly localised around 13 MeV, although some strength cannot be excluded in the upper part of the GDR distribution. This pattern might suggest some oblate contribution to the effective shape. This is also indicated by the contrast to the shape of the stretched and unstretched compo-

nents (solid lines) deduced from the photo absorption measurements for cold and (mostly) prolate Er nuclei [17]. In that case, the high-energy GDR component is a mixture of $\Delta I = 0$ and $\Delta I = 1$ transitions. In figure 15 the strength ratio of the observed $\Delta I = 0$, ± 1 components is different from the ratio for cold Er nuclei.

We further note that it is also possible to obtain an estimate of the width of the individual components without any analysis of the spectrum shape with the statistical model. From Fig. 15, we deduce $\Gamma(\Delta I = 0) \approx 4.0$ MeV and $\Gamma(\Delta I = \pm 1)$ ≈ 3.0–4.0 MeV. Finally, we can obtain an estimate of the *effective* deformation from the energy difference of the two components. We find $\beta \approx (E2-E1)/\langle E \rangle = 0.20$, in remarkable agreement with the predictions of the shape calculations for the equilibrium shape.

We conclude this section by remarking that we have not applied this difference procedure to the high angular momentum reactions leading to the formation of ^{161,162}Yb discussed in sect. 3.1. Such doubly exclusive measurements (for ^{160,161,162}Yb) using a new high-efficiency multiplicity filter (total efficiency $> 70\%$) consisting of 38 elements of BaF_2 arranged in a "castle" geometry will be discussed in a forthcoming publication [18].

4. Comparison to fluctuation theory and interpretation

4.1. Fluctuation theories for hot nuclei

Fig. 16 shows calculated contours of the free energy in the rotating frame $F = U - TS - \boldsymbol{I} \cdot \boldsymbol{\omega}$, for the nucleus ^{162}Yb at different temperatures (T) and rotational frequencies (ω), in terms of the deformation parameters β and γ described in sect. 3. The contours lines are spaced by 2 MeV, increasing radially outwards from the minimum. In the present case the calculations have been done within the framework of the Landau theory of shape transitions developed by Alhassid et al. [19]. In this approach the free energy may be written as

$$F(\beta, \gamma, T, \omega) = F(\beta, \gamma, T, \omega = 0) - \tfrac{1}{2}J_z\omega^2$$

$$= F_0(T) + A(T)\beta^2 - B(T)\beta^3 \cos\left(3\left(\gamma - \frac{2\pi}{3}\right)\right)$$

$$+ C(T)\beta^4 - \tfrac{1}{2}J_z\omega^2,$$

where J_z is the moment of inertia about the z-axis (assumed to be the axis of rotation)

$$J_z = J_0(T) - 2R(T)\beta \cos\left(\gamma - \frac{2\pi}{3}\right) + 2J_1(T)\beta^2$$

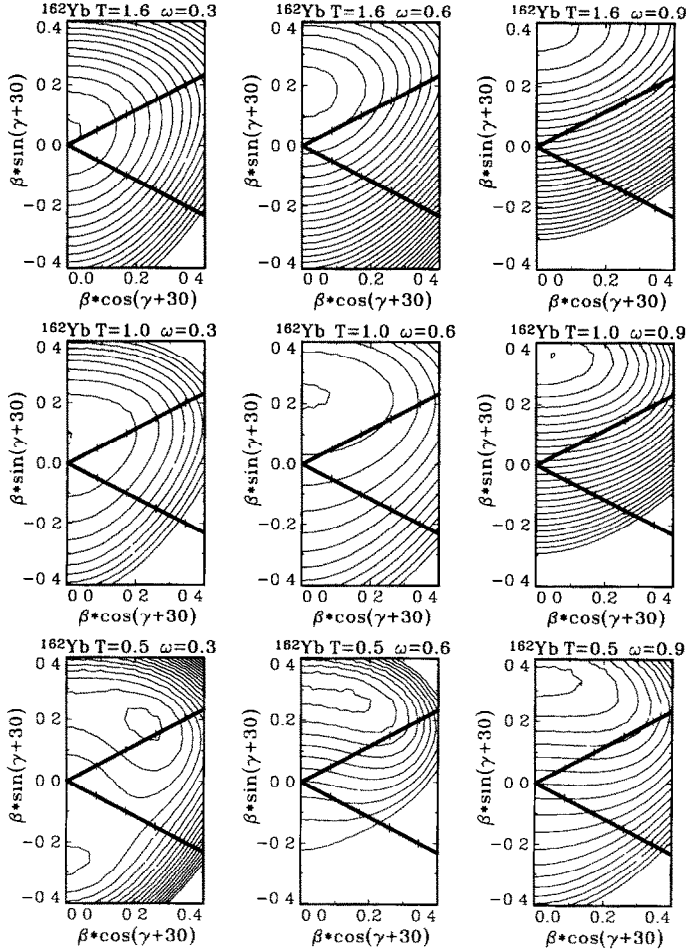$$+ 2D(T)\beta^2 \sin^2\left(\gamma - \frac{2\pi}{3}\right),$$

Fig. 16. Calculated contours of the free energy in the rotating frame for ^{162}Yb at different rotational frequencies and temperatures. Contours are spaced by 2 MeV.

where the coefficients A, B, C, J_0, R, J_1 and D vary smoothly with temperature. These coefficients are determined from fits to microscopic calculations (for example of the Nilsson–Strutinsky type). The parameters have been supplied to us by Alhassid [20]. A compilation of the A, B, C parameters as a function of T for rare-earth nuclei parameters is given by Bush [21]. In many cases it may be reasonable to use the rigid-body moments of inertia $(J_0 = 2/5M(R_0)^2$, $R = (5/16\pi J_0)^{1/2}$ and $J_1 = D = 0)$ at higher T. Note that we have rewritten the equations for F and J_z in terms of the γ parameter defined in the beginning of sect. 3 which differs from the convention of Alhassid by $+ \frac{2}{3}\pi$.

The figure illustrates the expected transition from well-deformed prolate shapes, near the ground state (panel at lower left), to oblate shapes of small deformation

at low rotational frequencies and of large deformation at higher ω occurring already at $T \approx 1$ MeV for these $N = 92$ nuclei. The figure also shows the increasing shallowness of the free energy surfaces which develops with increasing temperature suggesting that shape fluctuations will be important in these nuclei already at moderate T.

Another source of fluctuations which affects GDR angular distributions is due to variations of the angles which describe the orientation of the nucleus with respect to a given axis (for example the rotation axis or the direction of the total angular momentum). While shape fluctuations can play a major role in modifying both the effective GDR strength function and the GDR angular distribution, orientation fluctuations mostly affect the angular distribution.

In general we may consider the effect of fluctuations on the GDR properties in two extreme scenarios: the *fully adiabatic* model [22] and the *extreme motional narrowing* model [23]. The physical pictures underlying these two approaches are easy to understand. In the adiabatic model it is assumed that the nucleus spends sufficient time in each configuration (characterised by the deformation, shape and orientation variables) that the GDR sees that configuration as *static* for the time that it takes to damp the GDR into the compound nucleus states. As a consequence, the effective GDR strength function must be seen as an average, with a suitable statistical weight, over all the configurations that can be explored. In the motional narrowing scenario it is considered that the time scale for configuration changes may be short compared to the time needed for the GDR to adjust to a given configuration. As a consequence only part of the available phase space is explored. In the extreme motional narrowing model the GDR sees only the equilibrium configuration, thus effectively quenching all fluctuations. A determination of which of these models (or what intermediate model) is appropriate for describing the experiments thus carries important information on the time scales of the rearrangement of nucleonic configurations in hot nuclei. We remark that earlier work has indicated the need for an intermediate model in the $A = 100$ region [24,25] while data from the $A = 90$ region [26] and in the $A = 165$ [27,28] region at low T and I are consistent with the adiabatic model.

In Fig. 17 we illustrate the influence of fluctuations on the GDR strength function for various rotational frequencies and temperatures in the case of ^{162}Yb. In this figure the dotted line indicates the expected GDR strength function for the equilibrium deformation (this can then be associated with the extreme motional narrowing result). The dashed line show the strength function including only adiabatic shape fluctuations, while the solid line shows the result of considering adiabatic fluctuations of shape as well as orientation. Fig. 18 shows similar information for the GDR angular distribution.

We note that the GDR strength functions are not affected by orientation fluctuations and that shape fluctuations play a major role in smoothing the distributions at higher T. As far as the angular distributions are concerned we

concentrate the discussion on the magnitude of the predicted negative anisotropies in the range $E_\gamma = 11$–13 MeV. It is apparent that large negative anisotropies (around $A_2 = -0.15$ to -0.20) are predicted for all T and ω when only shapes fluctuations are included. The anisotropies increase only slowly with increasing rotation and temperature. A noteworthy feature is that the magnitude of the anisotropies corresponding to the equilibrium deformation are much smaller than those corresponding to those where an averaging over shapes has been done, except at the highest rotation and for situations close to the ground state. This behaviour reflects the strong role of *shape* fluctuations admixing large deformations into the effective shape. *Orientation* fluctuations obviously are very important, strongly attenuating the angular distribution at low rotational frequency. At high rotation, however, all curves converge suggesting that measurements of the angular distribution of GDR gamma rays at high angular momenta can give an almost model-independent picture of the shape of hot nuclei.

In the following we briefly describe the formalism we have used to generate Figs. 17 and 18.

At a given deformation and for a given shape we describe the GDR strength function as a superposition of three lorentzian functions each centred at a frequency given by the Hill–Wheeler formula

$$E_k = E_{\mathrm{GDR}} \exp\left[-\sqrt{\frac{5}{4\pi}}\, \beta \cos\left(\gamma - \frac{2\pi}{3} k \right) \right]$$

where $k = 1, 2, 3$ labels the principal axes (x, y, z) in the intrinsic frame and E_{GDR} is the average energy of the GDR determined from systematics. To each component we associate a width given by

$$\Gamma_k = \Gamma_{\mathrm{GDR}} \left(\frac{E_k}{E_{\mathrm{GDR}}} \right)^\delta$$

where $\Gamma_{\mathrm{GDR}} = 5$ MeV and [29] $\delta = 1.9$. We have in the present case neglected Coriolis splitting of the GDR components. This effect is however small (of order $\Delta\omega = 0.5$ MeV).

The angular distribution of the individual GDR components in the laboratory frame of reference depends on the multipolarity of the considered transition. The multipolarity is determined by the orientation of the plane of the considered vibration relative to the direction of the rotation axis. In general

$$S\!\left\{ \begin{array}{c} \Delta I = 0 \\ \Delta I = \pm 1 \end{array} \right\}(E_\gamma, \alpha) = S_0(E_\gamma) \left[1 + \left\{ \begin{array}{c} +0.50 \\ -0.25 \end{array} \right\} P_2(\cos \alpha) \right],$$
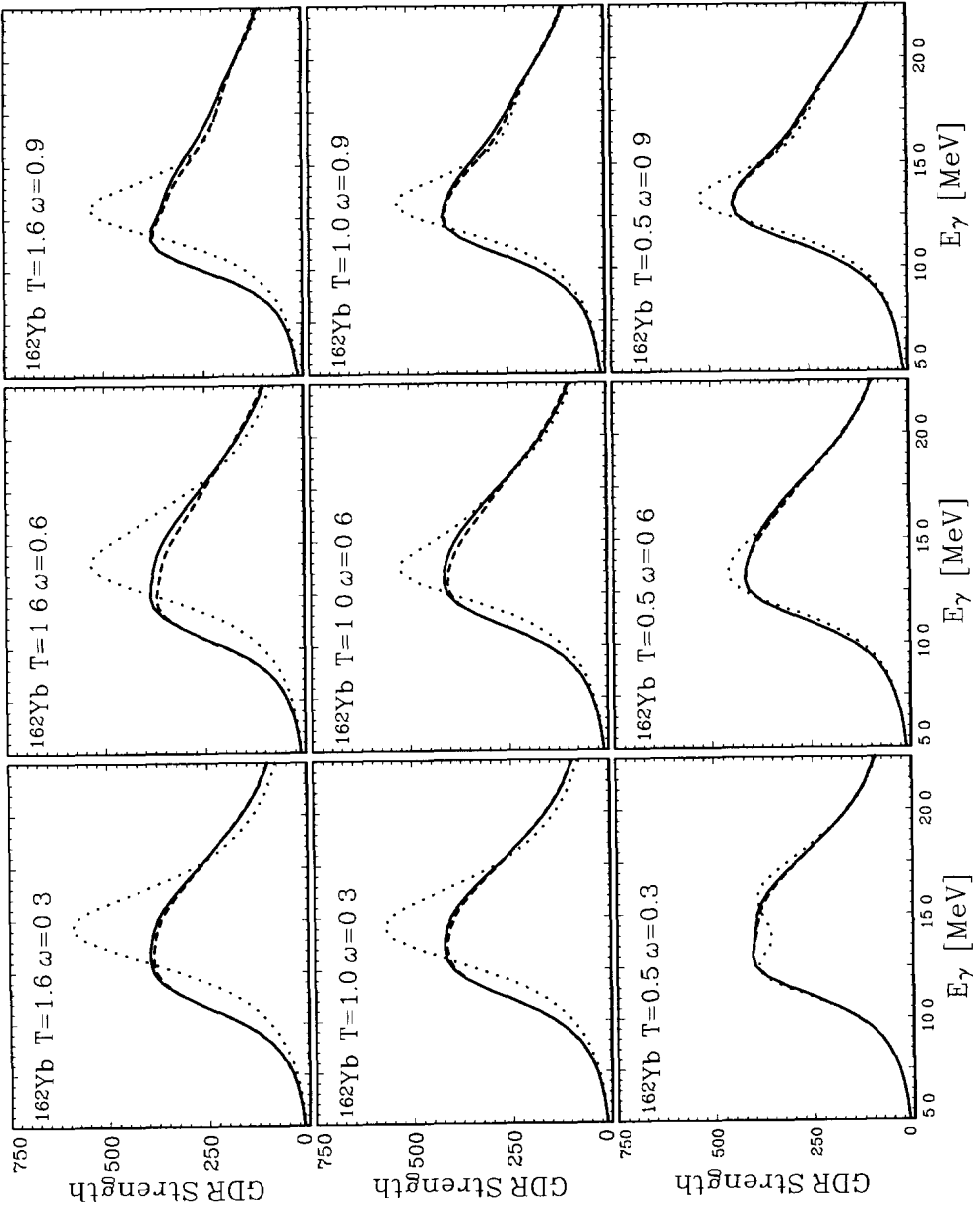
Fig. 17. Illustration of the effect of fluctuations on the GDR strength function calculated as described in sect. 4.2. Dotted line: equilibrium shape, dashed line: shape fluctuations only, solid line: shape and orientation fluctuations included.
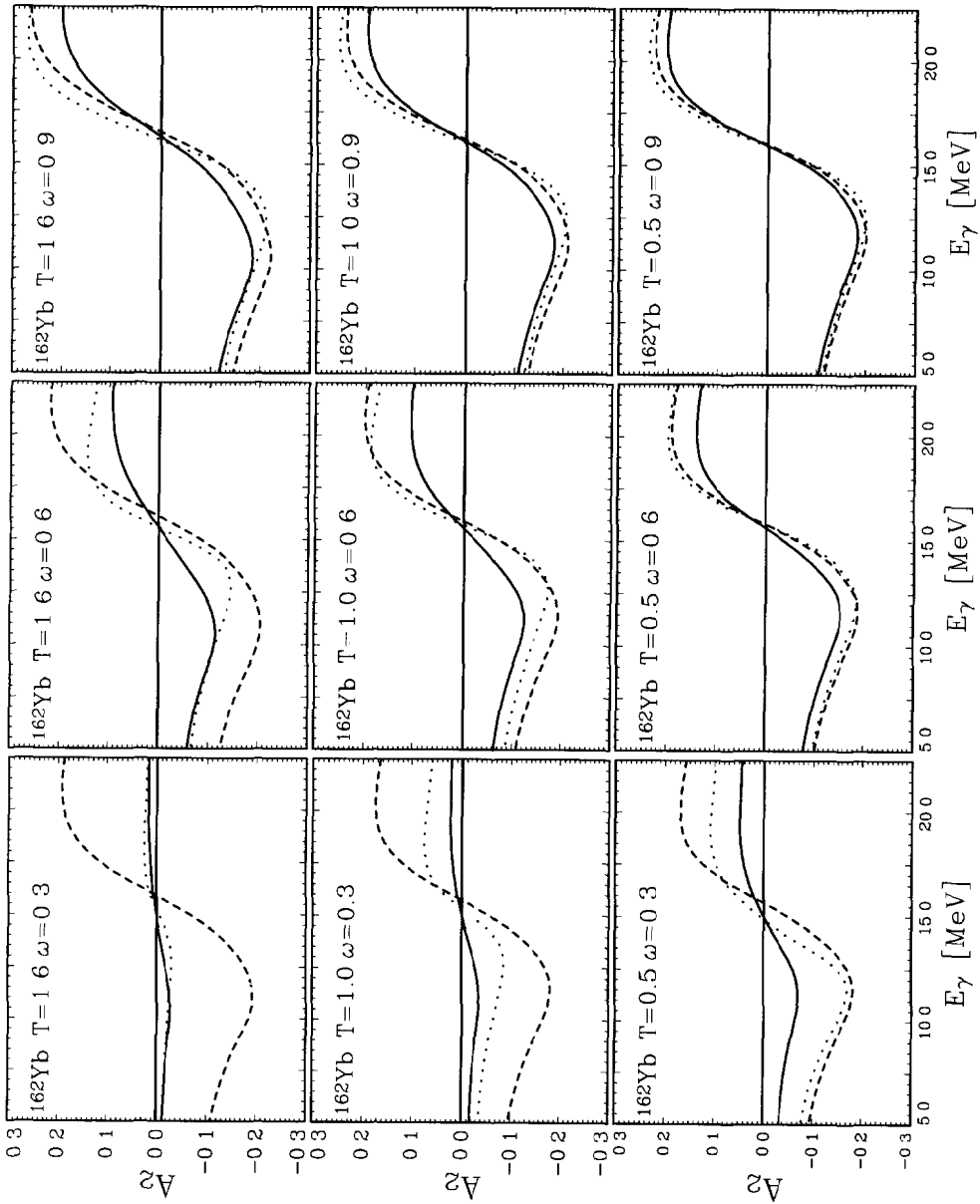
Fig. 18. Illustration of the effect of fluctuations on the GDR angular distribution calculated as described in sect. 4.2. Lines as in Fig. 17.

where α is the angle of observation of the gamma ray with respect to the beam axis, P_2 is the second Legendre polynomial and S_0 is the angle-independent part of the spectrum.

Neglecting the effect of Coriolis splitting an analytical expression for the angular distribution, with respect to the beam axis has been derived [30]

$$a_2(E_\gamma) = -\frac{1}{2}\left[\frac{\left(f_x(E_\gamma) + f_y(E_\gamma)\right)/2 - f_z(E_\gamma)}{f_x(E_\gamma) + f_y(E_\gamma) + f_z(E_\gamma)}\right]\left(\frac{3\cos^2\theta - 1}{2}\right)$$

$$+\frac{3}{8}\left[\frac{f_x(E_\gamma) - f_y(E_\gamma)}{f_x(E_\gamma) + f_y(E_\gamma) + f_z(E_\gamma)}\right]\sin^2\theta\,\cos 2\phi,$$

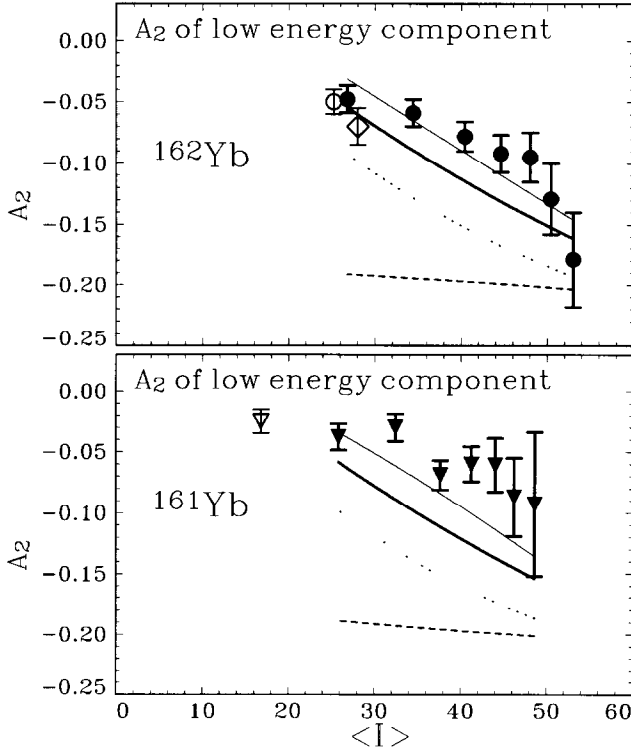

Fig. 19. Systematics of the magnitude of the GDR angular distribution coefficients (determined as the minimum value in the interval $E_\gamma = 11$–13 MeV) as a function of the angular momentum of the compound nucleus. Filled points refer to titanium induced reactions, open points to reactions with oxygen projectiles. Circles are for ^{162}Yb, triangles are for ^{161}Yb, a diamond is for the energy difference method. The lines are calculations showing the predicted trend in the case of fully adiabatic fluctuations in the deformation and orientation degrees of freedom (full drawn) and fully motional narrowed (dashed). The thin solid line shows the results of adiabatic calculations evaluated in the same energy range as the data (see discussion in sect. 4.2).

where $f_k (k = x, y, z)$ are the GDR strength functions (assumed to be of lorentzian shape with centroid E_k) corresponding to vibrations along the principal axes while θ and ϕ are the Euler angles describing the orientation of the rotational frequency vector with respect to the symmetry axis.

In the case of adiabatic fluctuations the effective GDR strength function at each T and ω can be estimated from

$$\langle f_{\mathrm{GDR}}(E_\gamma, T, \omega) \rangle = \frac{\int f_{\mathrm{GDR}}(E_\gamma, T, \omega, \beta, \gamma) \mathrm{e}^{-F(T, \omega, \beta, \gamma, \theta, \phi)/T} \, \mathrm{d}\tau}{\int \mathrm{e}^{-F(T, \omega, \beta, \gamma, \theta, \phi)/T} \, \mathrm{d}\tau}.$$

In practice we calculate the weighted average numerically over a grid in the parameters $\beta, \gamma, \theta, \phi$.

The free energy must in general take into account the orientation angles, thus

$$F(T, \omega, \beta, \gamma, \theta, \phi) = F(T, \omega = 0, \beta, \gamma)$$

$$-\tfrac{1}{2}\big(J_x \sin^2\theta \, \cos^2\phi + J_y \sin^2\theta \, \sin^2\phi + J_z \cos^2\theta\big)\omega^2$$

and the volume element over which the integration is carried out is

$$\mathrm{d}\tau = \beta^4 |\sin(3\gamma)| \sin \theta \, \mathrm{d}\beta \, \mathrm{d}\gamma \, \mathrm{d}\theta \, \mathrm{d}\Psi.$$

This volume element follows from the calculation of the jacobian associated with the transformation of the generalised quadrupole coordinates $(a^{0,\pm 1,\pm 2})$ to the set $(\beta, \gamma, \theta, \phi, \Psi)$. We remark that the averaging should be carried out over an interval of only $\Delta\gamma = 60°$ covering shapes ranging from prolate to oblate in order not to "double count" the averaging over orientations.

4.2. Interpretation of experimental results

In Fig. 19 we summarise the systematics of the A_2 coefficients obtained in the various experiments (see Figs. 12 and 14) as a function of the average angular momentum corresponding to the selected fold intervals. In preparing this figure we have chosen to display the minimum of the experimental A_2 distributions in the transition energy range $E_\gamma = 11$–44 MeV, determined by fitting the experimental distributions to a high-order polynomial. Features to be noted in Fig. 19 are; (i) the increase of the $|A_2|$ values with increasing angular momentum and (ii) the similarity between the values obtained for ^{161}Yb and for ^{162}Yb decays. In the case of ^{162}Yb we have also included the point associated with the energy differential measurement which has better defined excitation energy than the other points (see discussion in sect. 3.2).

In order to investigate the physical mechanisms underlying the trend of the data, we compare our measurements to calculated $A_2(E_\gamma)$ distributions for the equilibrium shape (dotted line), taking into account only shape fluctuations (dashed line) and taking into account both shape and orientation fluctuations (solid line). Such calculations are superimposed on the data presented in Figs. 12 and 14.

These calculations including the effect of fluctuations have been done within the formalism described in sect. 4.1. In order to compare experiment and theory we have constructed weighted averages of calculations for different T and ω in order to match the regions of phase space covered by the considered gamma-ray spectra. In doing this we have assumed the relations $T = [(E^* - E_{rot} - E_{GDR})/a]^{1/2}$ and $I = \mathcal{J}\omega$, where a is the level density parameter ($a = A/8$) and $\mathcal{J}$ is the rigid-body moment of inertia. The weight factors were obtained from statistical-model calculations.

It is apparent that an exact comparison of data and theory is difficult due to the different shapes of the calculated distributions and the fact that the theoretical distributions consistently fail to reproduce the data below $E_\gamma = 8.5$ MeV, in cases below 10 MeV. While we have no satisfactory explanation for this effect (which is seen in many other experiments) we note that this energy coincides with the neutron binding energy. Consequently gamma rays with transition energies below this energy are predominantly emitted at the end of the deexcitation sequence. However, the gamma-ray emitting nuclei should still have significant deformations and large alignment, and thus give rise to non-zero A_2 coefficients. More to the point is perhaps the fact that we are, at 8 MeV, far from the resonance peak (located at $E_\gamma = 11$–12 MeV for the lower GDR component). It is doubtful whether the vibration should be considered fully collective (and consequently well aligned) under these conditions. We remark that an isotropic low-energy part can be obtained by assuming (ad hoc) that the three GDR components are populated with unequal strengths, although we have no evidence for suggesting that is the case. We also note that the exact knowledge of the functional form of the E1 absorption cross section (lorentzian or other) is not important as long as the absorption cross sections along the main axes have the *same* functional form.

We compare in Fig. 19 the data points, obtained as described above, to the most negative value of the calculated A_2 distributions in the interval $E_\gamma = 11$–14 MeV. This yields the heavy solid curves displayed in Fig. 19. In order to take into account that the experimental and theoretical distributions behave differently, we also plot (for the calculations including shape and orientation fluctuations) the A_2 value of the theoretical distribution determined at the energy of the minimum of the experimental distribution. This is shown with the thin solid line.

The main aspects of this comparison are the following. The calculations (dotted line) for the equilibrium deformation and equilibrium orientation (the one that minimises the free energy), show an increase as a function of angular momentum in qualitative (but not quantitative) agreement with the data. The calculations

including only shape fluctuations (dashed line) are much less sensitive to angular momentum, reflecting the dominant role of the β^4 term in the averaging 5-dimensional volume element when the free energy surfaces are very shallow. The curves including both shape and orientation fluctuations are however able to reproduce the data rather well (in particular the calculation shown with the thin solid line obtained as described above), both insofar as trend and magnitude is concerned. We thus find good agreement between calculations assuming fully adiabatic fluctuations and the data in this mass region.

It is important to realise that the average excitation energies corresponding to the various selected angular momentum bins are different, due to the changing amount of energy bound in rotation (see Fig. 1). Consequently one should consider both angular momentum and excitation energy effects in interpreting the data shown in Figs. 12, 14 and 19. This can be done in a three-dimensional representation as the one shown in the top panel of Fig. 20. Also indicated on the figure is the region where the expected shape phase transition is expected to occur. It suggests that with the exception of the low-energy ^{161}Yb reaction, most of the sampled nuclei are oblate. We reached a similar conclusion from the analysis of the decomposed spectrum shown in Fig. 15. The bottom part of the figure shows for comparison the corresponding calculated (minimal) A_2 as a function of T and ω. The figure substantiates the surmise that, for nuclei in this mass and excitation energy range, the effects of temperature are small and that the changes seen in the angular distributions, reflecting the increase of the oblate deformation, are mostly due to angular momentum. The importance of the spin effects is shown also in another exclusive angular momentum gated data in this mass region [31–33].

5. Summary and conclusions

We have in this work studied with the use of angular momentum and excitation-energy selection methods in coincidence experiments how the angular distribution of the GDR photons from hot rotating nuclei depends on the angular momentum and excitation energy of the nucleus. We have investigated isotopes in the rare-earth region which are predicted to be "soft" against deformation changes, readily acquiring oblate shapes with increasing rotation and excitation energy. The data have been compared to model calculations describing shapes of hot and rotating nuclei and including thermally induced fluctuations of the shape and orientation of the nucleus within the scope of the fully adiabatic model and of the extreme motional narrowing model. These models represent opposite extremes in describing the coupling of the GDR to the quadrupole degrees of freedom of the atomic nucleus.

The main conclusions from this analysis are the following. (i) The description of this coupling as fully adiabatic reproduces the data well in this mass region over a
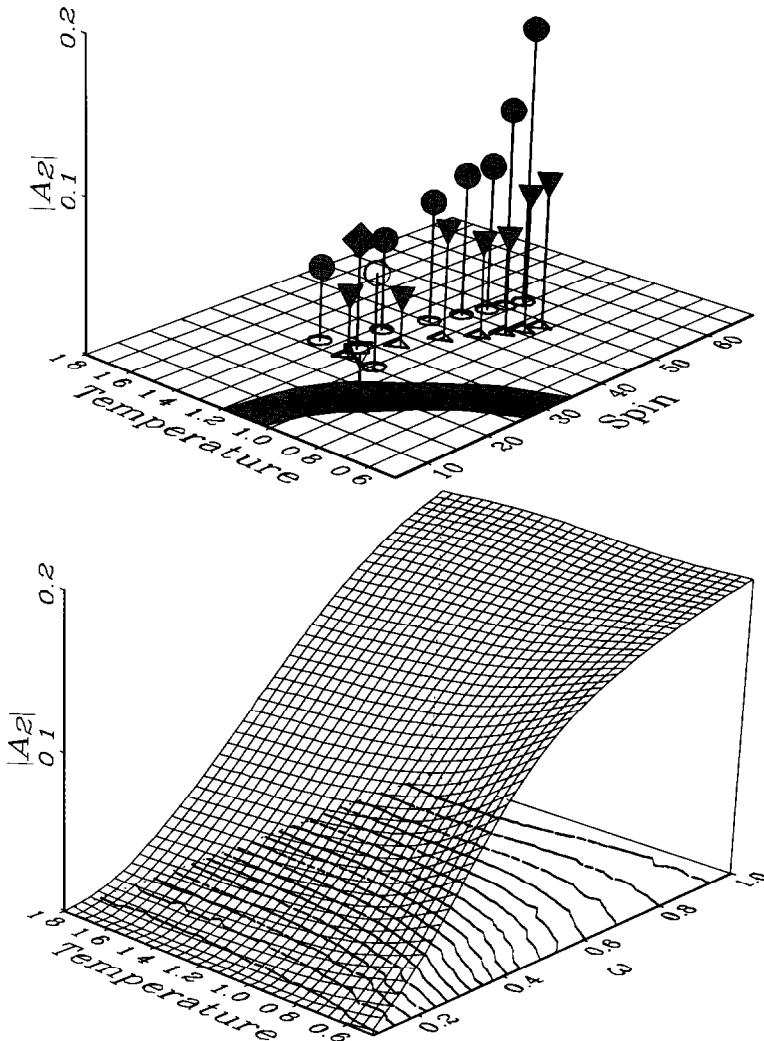
Fig. 20. *Top*: Three-dimensional representation of the systematics of the measured magnitude of the GDR angular distribution coefficients as a function of the average angular momentum and temperature of the emitting nuclei. The shaded area indicates the location of the predicted shape phase transition. Around this line the largest fluctuations are expected and consequently the smallest A_2 values. *Bottom*: Calculated distribution of minimum A_2 values as a function of temperature and rotational frequency, in the range corresponding (using the $I = \mathscr{J}\omega$ relation, where $\mathscr{J}$ is the rigid-body moment of inertia) to the top part. The lines on the temperature-ω plane connect the points with equal A_2 value and are spaced by 0.01.

span of excitation energies in the region of the predicted shape phase transition and covering a large interval in angular momentum. This behaviour is at variance with the one observed in region of light Sn isotopes (around $A = 110$) using the

same experimental apparatus and identical analysis procedures, where neither type of model calculations can reproduce the trend of the data. (ii) The data presented here substantiate the dominant role of orientation fluctuations in determining the angular distribution of the GDR and the strong angular momentum dependence of orientation fluctuations. (iii) At temperatures in excess of the predicted shape phase transition the data indicate that the influence of temperature on the observed angular distributions is modest. This has implications for the ongoing debate regarding the role of collisional damping in very hot nuclei (i.e. with excitation energies of several hundred MeV, see the discussion in ref. [1]). (iv) At large angular momenta the different fluctuation theories predict essentially the same angular distributions. This convergence suggests that the study of GDR angular distributions at very high rotation may provide a very direct view of the conditions prevailing in highly excited nuclear systems.

References

[1] J.J. Gaardhøje, Ann. Rev. Nucl. Part. Sci. 42 (1992) 483
[2] K.A. Snover, Ann. Rev. Nucl. Part. Sci. 36 (1986) 545
[3] J.J. Gaardhøje, C. Ellegard, B. Herskind and S.G. Steadman, Phys. Rev. Lett. 53 (1984) 148
[4] M. Kicińska-Habior, K.A. Snover, J.A. Behr, C.A. Gosset, J.H. Gundlach and G. Feldman, Phys. Rev. C45 (1992) 569
[5] P. Thirolf, D. Habs, D. Schwalm, R.D. Fischer and V. Metag, Nucl. Phys. A482 (1988) 93c
[6] A. Stolk, A. Balanda, M.N. Harakeh, W.H.A. Hesselink, J. Penninga and H. Rijneveld, Nucl. Phys. A505 (1989) 241
[7] A.M. Bruce, J.J. Gaardhøje, B. Herskind, R. Chapman, J.C. Lisle, F. Khazaie, J.N. Mo and P.J. Twin, Phys. Lett. B215 (1988) 237;
    A.M. Bruce et al., private communication
[8] D.R. Chakrabarty, M. Thoennessen, N. Alamanos, P. Paul, R. Schicker, J. Stachel and J.J. Gaardhøje, Phys. Rev. C36 (1987) 1886
[9] D.R. Chakrabarty, M. Thoennessen, S. Sen, P. Paul, R. Butsch and M.G. Herman, Phys. Rev. C37 (1988) 1437
[10] F. Camera, Ph. D. Thesis, University of Milano, 1992
[11] Helena multiplicity filter, NBI Annual Report 1992
[12] A. Holm, P. Høy-Christensen, D. Jerrestam, O. Christensen and L. Carlen, IEE, Trans. Nucl. Sci. NS-34, 4 (1987) 1008;
    D. Jerrestam, A. Forycki, A. Holm, P. Høy-Christensen and T. Jian Shen, Nucl. Instr. Meth. A285 (1989) 469
[13] M. Jääskeläinen, D.G. Sarantites, R. Woodward, F.A. Dilmanian, J.T. Hood, R. Jääskeläinen, D.C. Hensley, M.L. Halbert and J.H. Barker, Nucl. Instr. Meth. 207 (1983) 385
[14] A. Holm, unpublished, internal report NBI

[15] J.J. Gaardhøje, O. Andersen, R.M. Diamond, C. Ellegaard, L. Grodzins, B. Herskind, Z. Sujkowski and P.M. Walker, Phys. Lett. B139 (1984) 273

[16] A. Maj, J.J. Gaardhøje, B. Herskind, G. Sletten, J. Nyberg, A. Bracco, B. Million and M. Pignanelli, Phys. Lett. B291 (1992) 385

[17] B.L. Berman, At. Data Nucl. Data Tables 15 (1975) 319

[18] Z. Żelazny, J.J. Gaardhøje, W. Korten, A. Maj, T. Tveter, T. Ramsøy, A. Bracco, F. Camera, M. Matiuzzi, B. Million and M. Pignanelli, to be published

[19] Y. Alhassid, S. Levit and J. Zingman, Phys. Rev. Lett. 57 (1986) 539;
Y. Alhassid and B. Bush, Nucl. Phys. A509 (1990) 461

[20] Y. Alhassid, private communication

[21] B. Bush, Ph. D. Thesis, Yale University, 1987

[22] M. Gallardo, M. Diebel, T. Døssing and R.A. Broglia, Nucl. Phys. A443 (1985) 415

[23] B. Lauritsen, R.A. Broglia, W.E. Ormand and T. Døssing, Phys. Lett. B207 (1988) 238

[24] W.E. Ormand, P.F. Bortignon, R.A. Broglia, T. Døssing and B. Lauritzen, Phys. Rev. Lett. 64 (1990) 2254

[25] F. Camera, A. Bracco, B. Million, M. Pignanelli, J.J. Gaardhøje, A. Maj and A. Ataç, Phys. Lett. B293 (1992) 18

[26] Y. Alhassid and B. Bush, Phys. Rev. Lett. 65 (1990) 2527

[27] J. Pacheco, C. Yannouleas and R.A. Broglia, Phys. Rev. Lett. 61 (1988) 294

[28] Y. Alhassid, B. Bush and S. Levit, Phys. Rev. Lett. 61 (1988) 1926

[29] P. Carlos, H. Beil, R. Bergère, A. Leprêtre, A. Miniac and A. Veyssière, Nucl. Phys. A225 (1974) 171

[30] Y. Alhassid and B. Bush, Nucl. Phys. A514 (1990) 434

[31] A. Stolk, M.N. Harakch, W.H.A. Hesselink, H.J. Hofmann, R.F. Noorman, J.P.S. van Schagen, Z. Sujkowski, H. Verheul, M.J.A. de Voigt and D.J.P. Witte, Phys. Rev. C40 (1989) R2454

[32] S. Flibotte, B. Haas, P. Taras, H.R. Andrews, D.C. Radford and D. Ward, Nucl. Phys. A531 (1991) 205

[33] R.F. Noorman, J.C. Bacelar, M.N. Haraakeh, W.H.A. Hesselink, H.J. Hofmann, N. Kalantar-Nayestanaki, J.P.S. van Schagen, A. Stolk, Z. Sujkowski, M.J.A. de Voigt and A. van der Woude, Phys. Lett. B292 (1992) 257